PLOS COMPUTATIONAL BIOLOGY

RESEARCH ARTICLE

A novel machine learning based approach for iPS progenitor cell identification

Haishan Zhang[1,2☯], Ximing Shao[3☯], Yin Peng[4☯], Yanning Teng[1¤], Konda Mani Saravanan[1], Huiling Zhang[1], Hongchang Li[3]*, Yanjie Wei[1]*

1 Joint Engineering Research Center for Health Big Data Intelligent Analysis Technology, Center for High Performance Computing, Shenzhen Institutes of Advanced Technology, Chinese Academy of Sciences, Shenzhen, Guangdong, China, **2** University of Chinese Academy of Sciences, Shijingshan District, Beijing, China, **3** Shenzhen Key Laboratory for Molecular Biology of Neural Development, Guangdong Key Laboratory of Nanomedicine, Institute of Biomedicine and Biotechnology, Shenzhen Institutes of Advanced Technology, Chinese Academy of Sciences, Shenzhen, Guangdong, China, **4** Department of Pathology, Shenzhen University School of Medicine, Shenzhen, Guangdong, PR China

☯ These authors contributed equally to this work.
¤ Current address: China Merchants Bank Network Technology(Hangzhou) Co., Binjiang District, Hangzhou, Zhejiang, China
* hc.li@siat.ac.cn (HL); yj.wei@siat.ac.cn (YW)

Citation: Zhang H, Shao X, Peng Y, Teng Y, Saravanan KM, Zhang H, et al. (2019) A novel machine learning based approach for iPS progenitor cell identification. PLoS Comput Biol 15 (12): e1007351. https://doi.org/10.1371/journal.pcbi.1007351

Editor: Quan Zou, University of Electronic Science and Technology, CHINA

Received: August 19, 2019

Accepted: November 15, 2019

Published: December 26, 2019

Data Availability Statement: All relevant dataset files are available from the figshare database (DOI: https://doi.org/10.6084/m9.figshare.9685511).

Funding: This work is supported by the National Key Research and Development Program of China under Grant No. 2018YFB0204403 and 2016YFB0201305; National Science Foundation of China under grant no. U1435215 and 61433012; the Shenzhen Basic Research Fund under grant no. JCYJ20160331190123578, JCYJ20170413093358429 and

Abstract

Identification of induced pluripotent stem (iPS) progenitor cells, the iPS forming cells in early stage of reprogramming, could provide valuable information for studying the origin and underlying mechanism of iPS cells. However, it is very difficult to identify experimentally since there are no biomarkers known for early progenitor cells, and only about 6 days after reprogramming initiation, iPS cells can be experimentally determined via fluorescent probes. What is more, the ratio of progenitor cells during early reprograming period is below 5%, which is too low to capture experimentally in the early stage. In this paper, we propose a novel computational approach for the identification of iPS progenitor cells based on machine learning and microscopic image analysis. Firstly, we record the reprogramming process using a live cell imaging system after 48 hours of infection with retroviruses expressing Oct4, Sox2 and Klf4, later iPS progenitor cells and normal murine embryonic fibroblasts (MEFs) within 3 to 5 days after infection are labeled by retrospectively tracing the time-lapse microscopic image. We then calculate 11 types of cell morphological and motion features such as area, speed, etc., and select best time windows for modeling and perform feature selection. Finally, a prediction model using XGBoost is built based on the selected six types of features and best time windows. Our model allows several missing values/frames in the sample datasets, thus it is applicable to a wide range of scenarios. Cross-validation, holdout validation and independent test experiments show that the minimum precision is above 52%, that is, the ratio of predicted progenitor cells within 3 to 5 days after viral infection is above 52%. The results also confirm that the morphology and motion pattern of iPS progenitor cells is different from that of normal MEFs, which helps with the machine learning methods for iPS progenitor cell identification.

GGFW2017073114031767; Chinese Academy of Sciences grant under no. 2019VBA0009. We would also like to thank the funding support by the Shenzhen Discipline Construction Project for Urban Computing and Data Intelligence, Youth Innovation Promotion Association, CAS to Yanjie Wei. The funders had no role in study design, data collection and analysis, decision to publish, or preparation of the manuscript.

Competing interests: The authors have declared that no competing interests exist.

Author summary

Identification of induced pluripotent stem (iPS) progenitor cells could provide valuable information for studying the origin and underlying mechanism of iPS cells. However, it is very difficult to identify experimentally since there are no biomarkers known for early progenitor cells, and only after about 6 days of induction, iPS cells can be experimentally determined via fluorescent probes. What is more, the percentage of the progenitor cells during the early induction period is below 5%, too low to capture experimentally in early stage. In this work, we proposed an approach for the identification of iPS progenitor cells, the iPS forming cells, based on machine learning and microscopic image analysis. The aim is to help biologists to enrich iPS progenitor cells during the early stage of induction, which allows experimentalists to select iPS progenitor cells with much higher probability, and furthermore to study the biomarkers which trigger the reprogramming process.

Introduction

Induced pluripotent stem (iPS) cells are cells with embryonic-like state reprogrammed from mouse embryonic or adult fibroblasts by introducing the defined factors [1]. Since Takahashi and Yamanaka [1] first proposed the methods of reprogramming somatic cells to iPS cells, it has become an important method for clinical cell therapy, and revolutionized regenerative medicine [2], such as platelet deficiency [3], spinal cord injury [4], macular degeneration [5], Parkinson's disease [6] and Alzheimer's disease [7]. However, obstacles still remain in scientific and clinical applications for iPS cells because of potential tumorigenicity and low efficiency of reprogramming technique [8–10]. Tumorigenicity is attributed to the introduction of tumorigenic factors such as Oct4, Sox2, Klf4 and c-Myc, of which over-expression is generally associated with tumors. Inefficiency concerns low frequency for reprogramming cells, which is less than a small proportion of 5%. In some induction protocols, the ratio of progenitor cells during the early stage of reprogramming is even under 0.5%.

The above-mentioned obstacles are mainly due to poor understanding of molecular mechanisms in iPS cell reprogramming, which ultimately prevented this technology from a wide range of scientific and clinical applications. Theoretical mechanisms models are proposed such as two-step process model [11] and seesaw model [12], most of which focus on how factors such as Oct4, Sox2, Klf4, and c-Myc induce pluripotency. Experimental approaches based on epigenetic profiling, RNA screening or single-cell analysis for uncovering the mechanisms are limited by the low reprogramming efficiency or the lack of biomarkers for progenitor cells [13–20].

Recent studies found that iPS progenitor cells differed from normal MEFs in morphology, motion or proliferation rate. Smith et al. [21] found that iPS progenitor cells showed smaller cellular area and higher proliferative rate than normal MEFs via time-lapse imaging. Zhang et al. [22] also found that iPS cells exhibited distinct morphology features and different proliferative rate compared with larger and quiescent differentiated cells. Li et al. [23] showed the mesenchymal-to-epithelial transition, a process with significant morphological changes, was a key cellular mechanism for induced pluripotency. Megyola et al. [24] demonstrated that migratory motions for progenitor cells were often distinct in direction and distance to bring distant progenitor cells together. Most of these studies relied on time-lapse microscopy, which allowed studying/tracing cellular events in early reprogramming by direct observation [24]. Since iPS progenitor cells exhibit unique morphology and motion features, computational methods, especially machine learning based methods, could provide an alternative method to

identify iPS progenitor cells in the early stage of reprogramming process through learning the morphology and motion patterns of iPS progenitor cells.

Usually cell detection, segmentation and tracking are firstly required for computational methods to study cell images. Li et al. [25] proposed DCELLIQ for cell nuclei tracking based on neighboring graph and integer programming techniques. Dzyubachyk et al. [26] relied on coupled active surfaces algorithm for cell segmentation and tracking in time-lapse fluorescence microscopy images. Maška et al. [27] presented a tracking method for fluorescent cells based on coherence-enhancing diffusion filtering and Chan-Vese model. Türetken et al. [28] proposed an integer programming approach for tracking elliptical cell populations in time-lapse image sequences. Payer et al. [29] developed a recurrent fully convolutional network architecture for instance segmentation and tracking with training network using an embedding loss based on cosine similarities.

Recently machine learning/deep learning methods have been extensively developed for the prediction and study of cell images. Using cell images, Erdmann et al. [30] introduced a machine learning based framework for image-based screen analysis. Valen et al. [31] tried to solve cell image segmentation problem utilizing deep convolutional neural networks, and demonstrated its effectiveness in segmenting fluorescent images of cell nuclei. Chen et al. [32] achieved high classification accuracy in label-free white blood T-cells against colon cancer cells via a deep learning method. Similarly with a deep convolutional neural network method, Kraus et al. [33] analyzed the microscopic images for yeast cells and other pheromone-arrested cells, and Gao et al. [34] achieved a high ranking in the human epithelial-2 cell image classification competition hosted by ICPR2014. Together with principal component analysis, machine learning method can be used to infer regulatory network patterns underlying stem cell pluripotency [35]. The ability of machine learning has been demonstrated with its extensive application for cellular image data, however, it has been seldom used in the identification of iPS progenitor cells in the early stage.

In this article, we propose a machine learning based approach to detect iPS progenitor cells during the early stage of reprogramming. Given the cell images recorded via live-cell imaging system during the reprogramming process, the paper aims to identify iPS progenitor cells against normal MEFs in the same stage. The ratio of iPS progenitor cells to normal MEFs is usually below 5%, which makes the identification problem very difficult. In the paper we use Imaris, a software from Bitplane, to analyze and process microscopic cell images from live-cell imaging system. Surpass, a module of Imaris is then used to extract cell numerical information in the same time period. We then develop a machine learning method for identification of iPS progenitor cells based on the extracted morphological and motional features. The prediction model is built with XGBoost based on the selected six types of features and time windows. In our method, cell division is not considered, and frames contained in selected time windows are uniform. The model performance is evaluated by three different validation methods. When tested on labeled datasets with a ratio of about 1:5 between progenitor cells and normal MEFs, the prediction precision of iPS progenitor cells is above 52% during the first 1–3 days of reprogramming after adding iCD1 medium. The image-based machine learning method allows experimentalists to select iPS progenitor cells with much higher probability, and furthermore to study the biomarkers which trigger the reprogramming process.

Materials and methods

The workflow used in the paper is presented in **Fig 1**, which mainly includes feature extraction, preprocessing with missing values, feature selection, machine learning for training and validation. In this workflow, we acquire time-lapse images through experiments firstly, then

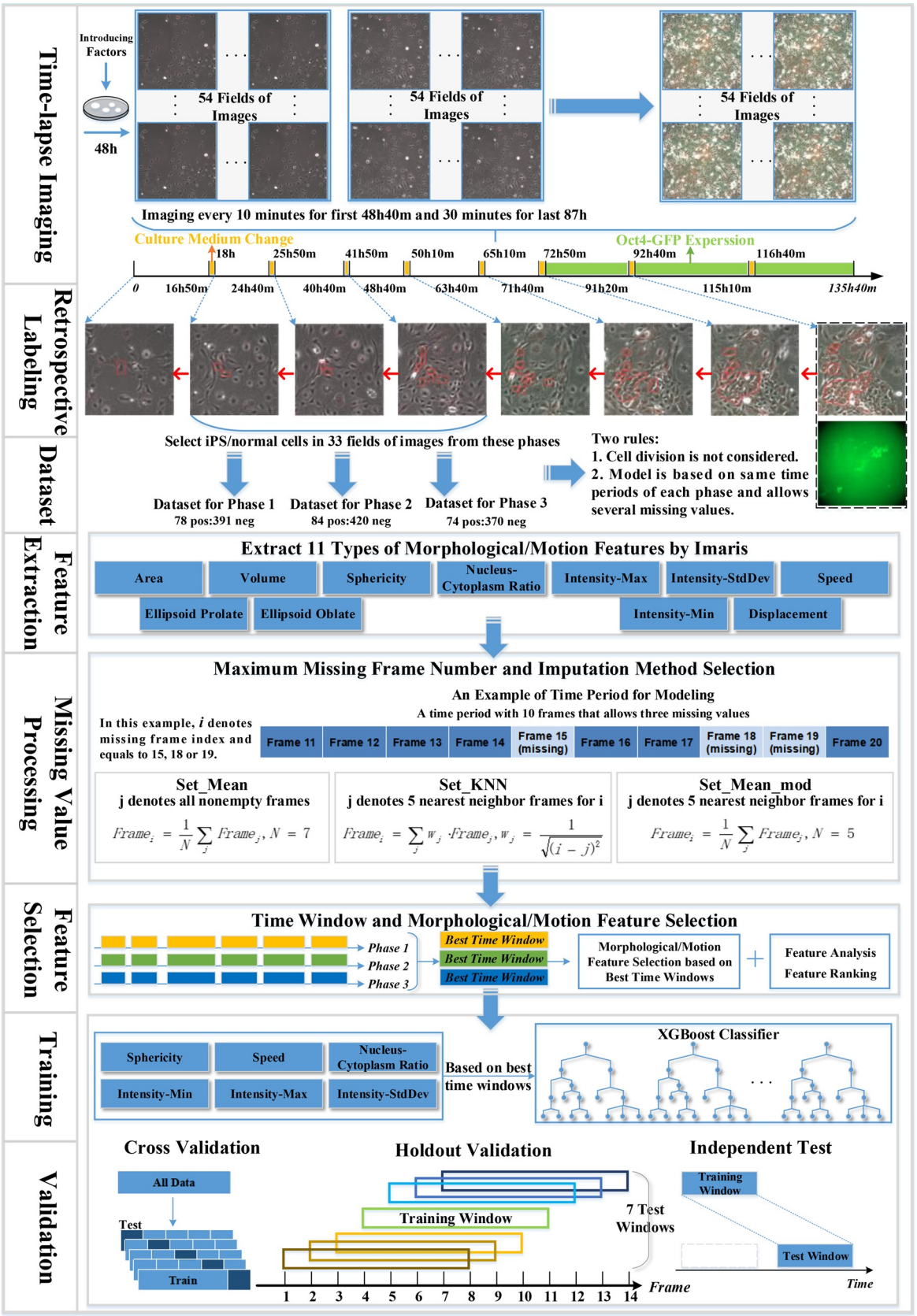
Time-lapse Imaging
Introducing Factors
48h
54 Fields of Images
54 Fields of Images
54 Fields of Images
Imaging every 10 minutes for first 48h40m and 30 minutes for last 87h
Culture Medium Change
Oct4-GFP Expression
18h
25h50m
41h50m
50h10m
65h10m
72h50m
92h40m
116h40m
0
16h50m
24h40m
40h40m
48h40m
63h40m
71h40m
91h20m
115h10m
135h40m
Retrospective Labeling
Select iPS/normal cells in 33 fields of images from these phases
Dataset
Dataset for Phase 1
78 pos:391 neg
Dataset for Phase 2
84 pos:420 neg
Dataset for Phase 3
74 pos:370 neg
Two rules:
1. Cell division is not considered.
2. Model is based on same time periods of each phase and allows several missing values.
Feature Extraction
Extract 11 Types of Morphological/Motion Features by Imaris
Area
Volume
Sphericity
Nucleus-Cytoplasm Ratio
Intensity-Max
Intensity-StdDev
Speed
Ellipsoid Prolate
Ellipsoid Oblate
Intensity-Min
Displacement
Missing Value Processing
Maximum Missing Frame Number and Imputation Method Selection
An Example of Time Period for Modeling
A time period with 10 frames that allows three missing values
In this example, i denotes missing frame index and equals to 15, 18 or 19.
Frame 11
Frame 12
Frame 13
Frame 14
Frame 15 (missing)
Frame 16
Frame 17
Frame 18 (missing)
Frame 19 (missing)
Frame 20
Set_Mean
j denotes all nonempty frames
$Frame_i = \frac{1}{N}\sum_j Frame_j, N = 7$
Set_KNN
j denotes 5 nearest neighbor frames for i
$Frame_i = \sum_j w_j \cdot Frame_j, w_j = \frac{1}{\sqrt{(i-j)^2}}$
Set_Mean_mod
j denotes 5 nearest neighbor frames for i
$Frame_i = \frac{1}{N}\sum_j Frame_j, N = 5$
Feature Selection
Time Window and Morphological/Motion Feature Selection
Phase 1
Phase 2
Phase 3
Best Time Window
Best Time Window
Best Time Window
Morphological/Motion Feature Selection based on Best Time Windows
Feature Analysis
Feature Ranking
Training
Sphericity
Speed
Nucleus-Cytoplasm Ratio
Intensity-Min
Intensity-Max
Intensity-StdDev
Based on best time windows
XGBoost Classifier
Validation
Cross Validation
All Data
Test
Train
Holdout Validation
Training Window
7 Test Windows
1 2 3 4 5 6 7 8 9 10 11 12 13 14
Frame
Independent Test
Training Window
Test Window
Time

Fig 1. Flow chart of the machine learning based approach for iPS progenitor cell identification. In time-lapse imaging, we record the reprogramming process periodically among 54 fields after 48h of viral infection. For retrospective tracking, the figure only shows the reprogramming lineage images of the first frame of all eight phases. Only datasets from phase 1, 2 and 3 are used for model training and testing.

https://doi.org/10.1371/journal.pcbi.1007351.g001

we recognize iPS progenitor cells and normal MEFs by tracing images retrospectively to generate datasets. Next, we generate 11 types of morphology and motion features with Imaris software. After the feature extraction, we perform time window selection and a two-step feature selection. Finally, we build the prediction model based on the selected six types of features and six time windows. The machine learning algorithm for modeling is XGBoost, a gradient boosting tree [36]. In the following sections, we will describe each step of our workflow in detail.

Cell culture and generation of iPS cells

Mouse embryonic fibroblasts (MEFs) are derived from E13.5 embryos carrying the Oct4 promoter-driven GFP reporter gene [37] and maintained in DMEM (HyClone) supplemented with 10% FBS (Gibco). To generate iPS cells, MEFs within two passages are seeded at a density of 5×10^4 cells/well in 6-well plates and cultured overnight. The next day, MEFs are infected with retroviral supernatants containing the DsRed gene and three reprogramming factors (Oct4, Sox2, Klf4) twice in a 48h process. After 48h of infection, iCD1 medium [38] is changed every day to achieve high reprogramming efficiency. iPS cell colonies are obtained 5–7 days post-treatment in iCD1 based on the Oct4-GFP expression.

Time-lapse imaging

Reprogramming process is recorded using an Olympus IX81 live cell imaging system equipped with a 10× UPlanFL objective, iXon3 EMCCD Camera. The date on which viral supernatants are removed and iCD1 mediums are added is defined as Day 0. From Day 0, MEFs images are taken for a total time of 135 hours and 40 minutes. For the first 48 hours and 40 minutes, both bright-field and red fluorescence images are acquired at 10-minute intervals. After two days of the dual-channel imaging, a green fluorescence channel is added to indicate the expression of Oct4-GFP and acquisition interval is adjusted to 30 minutes. Motorized Stage Control is used to follow cells in the same field and a total of 54 fields are selected at each time for further analysis.

Cell images taken within the first 48 hours and 40 minutes since Day 0 are used to construct the dataset because after this time the Oct4-GFP is added to identify the progenitor cells experimentally and the paper tries to identify/predict progenitor cells using computational methods as early as possible.

Cell segmentation and numerical feature extraction

The original files are time-lapse microscope images in TIFF format, whose pixels are 770 * 746 and the actual size is 1000 microns * 967 microns. Because some fields do not show distinct Oct4-GFP signals, resulting in no signals for iPS cells in these fields, we only use images from 33 fields for modeling. Imaris (Version 7) software is used to segment cells in the images of these 33 fields and extract the corresponding numerical features for the segmented cells. During this process, the parameter values of cell and nucleus intensity are set the same for all the cells in each field, and cell tracking duration of greater than 5000s is used. Imaris utilizes red fluorescent channel for cell segmentation and tracking. The image segmentation is based on the Watershed Algorithm, which is very sensitive to weak edges and intensity in images.

Features are computed for each segmented/identified cell image at different time frames by Imaris, and these features denote the morphological and movement information of the segmented cells during reprogramming. Overall 11 types of features are extracted (volume, area, sphericity, ellipsoid-prolate, ellipsoid-oblate, nucleus-cytoplasm volume ratio, displacement, speed, Intensity-StdDev, Intensity-Max, Intensity-Min) and each type contains features in several frames of the selected uniform time windows. The detailed list of features is presented in Part 1 of the S1 File.

Cell image dataset generation

Cell image datasets for machine learning consist of normal MEFs cell images and progenitor cell images within the first 48 hours and 40 minutes. The datasets will be used by our machine learning method in the training and testing processes.

As MEFs used for iPS reprograming carries the Oct4 promoter-driven GFP reporter gene (Oct4-GFP), experimentally generated iPS cells can be determined by Oct4-GFP expression signal, which cannot be observed until the seventh day after transfection with Yamanaka's factors. Cells showing green fluorescence in images are considered as iPS cells. The identified iPS cells were then traced retroactively to their source MEFs within the first 48 hours and 40 minutes based on the live-cell images (Fig 1). These characterized MEFs were defined as iPS progenitor cells while the other MEFs were considered as normal MEFs. Due to three one-hour iCD1 medium changes, the total reprogramming period is divided into four periods, the first period is 16 hours and 50 minutes long, from 18 hours to 24 hours and 40 minutes denoted as phase 1 in the paper, the second from 25 hours and 50 minutes to 40 hours and 40 minutes denoted as phase 2, and the third from 41 hours and 50 minutes to 48 hours and 40 minutes denoted as phase 3. In this paper, we focus on these three periods (phases 1, 2 and 3) only because of tiny ratio for iPS progenitor cells in the first 16 hours and 50 minutes, which is even less than 2%.

Two rules are applied in the paper for generating the cell image datasets, (1) cell division is not considered; (2) frames from the same window of each phase are selected for modeling among uniform time periods. When cell division is taken into account, features in the mother cell and its daughter cells are not comparable. For example, the area of mother cell is much bigger than that of its daughter cells, thus the machine learning model will fail to process this cell. The second rule guarantees that time dimension (time period and length) for the cell image data samples should be uniform.

For each cell, not every image in different frames can be identified by Imaris due to the fact that different parameter settings (cell or nucleus intensity threshold, cell tracking duration) by Imaris will lead to different segmented cell images in a frame. This results in cell image data missing in some frames, thus our method allows a certain number of missing cell images in the selected uniform time periods and tries to find the maximum number of continuous cells images in this uniform time period.

Overall three cell image sets are generated for three phases, each with an approximately 1:5 ratio between progenitor cell images and normal MEFs cell images. For phase 1, 78 IPS progenitor cells and 391 normal MEFs are labeled; for phase 2, 84 IPS progenitor cells and 420 normal MEFs are labeled; for phase 3, 74 IPS progenitor cells and 370 normal MEFs are labeled. Each of these three initial cell image sets are divided into the training and test sets: 70% of cell images for each time phases are selected randomly as training set with the remainder (30%) as test set. The ratio between progenitor cell images and normal MEFs cell images is kept approximately 1:5 for these training and testing sets. For the training sets, there are 55 iPS progenitor cells and 274 normal MEF cells in phase 1, 59 iPS progenitor cells and 294 normal MEF cells in phase 2, as well as 52 iPS progenitor cells and 259 normal MEF cells in phase 3.

In this paper, the initial cell dataset is used for cross-validating the proposed method, and the training dataset is used for missing value processing and feature selection. For different analytic steps, the specific data sample size depends on the time period from which the data has been collected. Numerical features are calculated for all cell images in the datasets and saved in CSV files. All datasets are standardized utilizing z-score.

Missing values processing

Processing missing values for the cells in the corresponding frames is an important step for our model. Imaris cannot continuously identify all the cells in the frame due to different parameter settings or complex three-dimensional cell environment. This implies that there exists a certain number of cell images with missing feature values in the uniform time periods. A certain number of missing images in the frames are permitted for cells to guarantee a modest data size, and missing cell features are estimated with an imputation method. To choose the most appropriate approach, we first analyze the impact of the number of missing frames on the model, and then analyze the effect of three different imputation methods under the corresponding missing frame numbers. Details for the three imputation methods are as follows:

- *set_mean*. The missing value is set to the average value of all nonempty frames for a specific type of feature in its sample from the selected time window.
- *set_KNN*. The missing value is set to the weighted average value of five nearest nonempty neighbor frames for a specific type of feature in its sample. The calculation of weight refer to the weight calculation method used by k-Nearest Neighbor (KNN) algorithm. The formula is as

$$\text{Missing value}_{\text{frame}_i} = \sum_j w_{frame_j} \cdot feature_{frame_j}, w_{frame_j} = \frac{1}{\sqrt{(i-j)^2}} \quad (1)$$

where j represents the index of five nearest neighbor frames for missing frame i.

- *set_mean_mod*. Missing value is set to the average value of five nearest nonempty neighbor frames for a specific type of feature in its sample.

Time window and feature selection

Because of the two rules used in dataset generation (Section **Cell image datasets generation**), although images are provided up to 49 hours, it is unable to construct the model based on the whole period. From a total of 49 hours, numerous time periods can be chosen, and the model needs to select best time windows among all these eligible time periods. Time window selection includes start frame selection and window length selection. Start frame represents the moment that the time window starts from, and window length represents frame number that the time window contains. For each time window with a selected time frame and window length, we train and validate the proposed method on the corresponding dataset generated. Validation is performed with 5-fold cross validation and the evaluation metric is precision.

Morphological and motion feature selection is used to improve the performance. Since it is difficult to guarantee image recording time to be accurately consistent for every batch through experiments, model performance needs to be robust among wider time periods. Every type of features contains multiple frames of features from the corresponding best time windows. Features in a time window are treated as a bundle so we can learn the dynamic cell growth process.

There are two steps for feature selection. The first step is recursive feature elimination. Firstly, we use all 11 types of features to train the model with 5-fold cross validation and calculate its precision as initial unimportance score. Then we delete each type of feature at a time and obtain 11 precision values as new unimportance scores. We compare every new score with the initial score, and remove the feature type with the largest unimportance score higher than initial score. The recursive process will be repeated on feature set until the model performance can be no longer improved or there is no feature. We then rank the importance of all 11 types of features and delete the least important feature types. Second, we calculate the Pearson correlation coefficient for the selected feature types from step 1 to remove the highly correlated features with a correlation coefficient of 0.60 or above.

Machine learning model and validation

XGBoost, a Boosting algorithm, is used in this paper for feature selection and iPS cell recognition. XGBoost integrates many weak tree-classifiers together to form a strong classifier. This algorithm applies numerous strategies to prevent overfitting, and it is widely utilized in data science such as cell analysis [39–43]. Hyperparameters of XGBoost are tuned using grid-search for model training with selected features and best time windows.

For model validation, firstly we use 5-fold cross-validation on the initial cell image datasets from the time windows of the three phases. Dataset generated from initial cell-sets contains about 70 iPS cells for each phase. The ratio of iPS cells and normal MEFs keeps as 1:5 in each dataset.

In order to test the model's ability/robustness to predict the iPS progenitor cells around the neighborhood of the corresponding training time window, holdout validation is performed. Because iCD1 medium change is operated manually during the experiments, it is impracticable to guarantee that for per batch data the duration of medium change is accurately consistent with the existing data. This inconsistency might lead to a non-exact match between the timeline after medium change and the timeline used in the model training process. The holdout validation is designed as follows, for the model trained on time window *i~j*, we examine the model's performance on several neighbor time windows, including time windows *i-3 ~ j-3*, *i-2 ~ j-2*, *i-1 ~ j-1*, *i ~ j*, *i+1 ~ j+1*, *i+2 ~ j+2*, and *i+3 ~ j+3*, where *i* represents start time frame of the window and *j* represents the terminal frame. The training dataset from time window *i~j* is generated from the initial training image data sets (70% of the initial total dataset), and test datasets of the seven neighbor time windows are generated from the test datasets (30% of the initial total dataset).

Moreover, in order to further test our model's ability to predict the iPS progenitor cell on a time window which doesn't overlap with the window in the training process, an independent test is performed. Model performance is tested on time windows which are far away from the training time windows. Since we have three time phases, we first select test time windows in phase 2 and 3 for the models trained on time windows of phase 1 and 2 respectively. For testing our model developed for phase 3, we select the independent test time windows also in phase 3, but without any overlap with the corresponding training time windows.

Evaluation metrics

In this paper, precision is mainly used for evaluation defined as,

$$precision = \frac{TP}{TP + FP}$$

where TP and FP represent the number of true positive and false positive prediction. This

metric evaluates the accuracy for the positive sample predicted by the model. Biologists need a cell sample set enriched with true iPS progenitor cells so that in the early stage of reprogramming progenitor cells can be studied with high probability.

Results and discussion

Missing frames processing and imputation method

First, the effect of missing frames and imputation methods on the model's performance was analyzed. Experiment for missing value was performed under six kinds of missing frame numbers, which were numbers below or equal to five, four, three, two, one and zero. Model performance was tested for each missing frame number with three imputation methods on time periods of two window lengths (10 and 19 frames) located in three phases, which were time period/window 19h30min ~ 21h10min from phase 1 (TP1), 25h50min ~ 27h30min from phase 1 (TP2), 41h50min ~ 43h30min from phase 2 (TP3), 18h10min ~ 21h20min from phase 2 (TP4), 26h ~ 29h10min from phase 3 (TP5) and 42h ~ 45h10min from phase 3 (TP6).

Two window lengths (10 and 19 frames) were selected because a reasonable number of continuous cell images could be traced. A short window would have more data but the motion and morphological pattern of iPS progenitor cells could not be learned, while a long window would result in a much smaller dataset. For each length, we chose three time windows randomly to study whether different lengths would affect model performance under uniform missing frame number. Datasets were generated from the training datasets, which were about 52~59 iPS cells and 259~294 normal MEFs for time windows with 10 frames, 43~50 iPS cells and 238~264 normal MEFs for time windows with 19 frames. Model was evaluated by the average precision with 5-fold cross validation over 20 times.

Fig 2 shows the comparison results of different missing frame numbers and imputation methods. For each missing number and imputation method, Fig 2A describes the average precision over six time windows (TP1 to TP6), indicated by blue boxes for set_KNN, red boxes for set_mean and green boxes for set_mean_mod. Also shown in Fig 2A is the average precision over all three imputation methods, indicated by grey boxes. Fig 2B describes the standard deviations of the corresponding precision values in Fig 2A. Detailed precision for all six time periods (TP1~TP6) are provided in Fig A of the S1 File.

Fig 2A shows that precision is higher when several missing frames are allowed. For missing frame number of 0, the average precision of all method is only 0.585 and all the average precision of non-zero missing frame numbers are higher than 0.585. Fig 2A also shows that the maximum average precision of all methods is about 0.632 under missing frames of 4, 4.7% higher than precision under no missing frames and 0.9% higher than precision under missing frame number of 2. On one hand, the size of the dataset is larger when missing value is permitted, on the other hand, the missing frame may introduce new pattern for classification because iPS progenitor cells proliferate more frequently than normal MEFs, and cell division can partly result in missing value. When cells divide at a certain frame in their time periods, the feature values of all subsequent frames are missing.

In Fig 2B, the maximum standard deviation of all methods as indicated by gray box is 0.061 under missing 4 frames. For each specific method, the maximum standard deviation is 0.081 for Set_mean under 5 missing frames. The precision with two missing frame numbers has the minimum standard deviation for all method (0.048 as indicated by gray boxes) and at the same time it is also very close to the maximum precision (0.623 compared with the maximum value of 0.632 in Fig 2A). In addition, Set_mean_mod shows the minimum standard deviation of all 3 imputation methods for all missing frame numbers (indicated by green boxes), an indication of stable performance. Although Set_mean_mod also shows smallest standard deviation

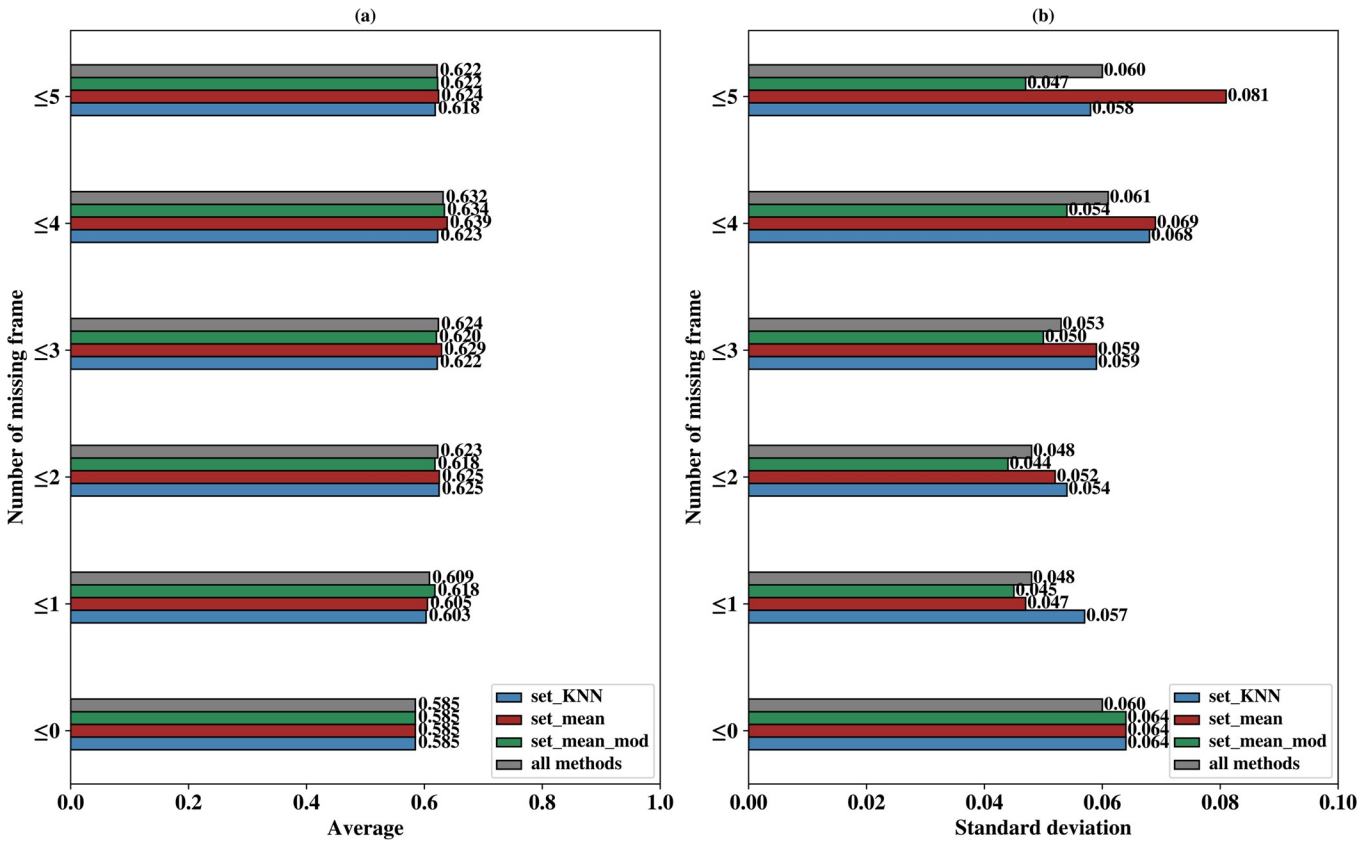

Fig 2. Model comparison for different missing frame number and imputation methods. (a) shows the average precision over six time periods (TP1 to TP6) for each missing frame number and imputation method set_KNN (colored as blue), set_mean (colored as red), set_mean_mod (colored as green) and all three imputation methods (colored as gray). (b) shows the standard deviation, as a function of missing frame number, of imputation method set_KNN (colored as blue), set_mean (colored as red), set_mean_mod (colored as green) and all three imputation methods (colored as gray).

https://doi.org/10.1371/journal.pcbi.1007351.g002

for missing frame number of 1, its precision value of missing frame number is smaller than that of missing frame number of 2. Therefore, we use missing frame number less than or equal to two and select imputation method as set_mean_mod in our model.

Time window selection

Time window selection was performed to select best time windows with high precision for each phase. Since Imaris could not detect all cell images in every frame, the whole time periods of three phases were divided into numerous time windows. For time window selection (including start frame and window length), we set start frame to 21 time points which were 18h20min, 18h40min, 19h, 19h20min, 19h40min, 20h, 20h20min, 26h10min, 26h30min, 26h50min, 27h10min, 27h30min, 27h50min, 28h10min, 42h10min, 42h30min, 42h50min, 43h10min, 43h30min, 43h50min, 44h10min in three phases. Meanwhile, we set window length to 12 different values including 7, 9, 11, 13, 15, 17, 19, 21, 23, 25, 27 and 29 frames. For the total of 252 (12 times 21) time windows, we first generated datasets for each time window with 11 types of morphological/motion features. All datasets were generated based on the training dataset and contained about 38~59 iPS progenitor cells and about 190~295 normal MEFs. Then we selected the optimal time window through 5-fold cross-validation based on 20 XGBoost runs.

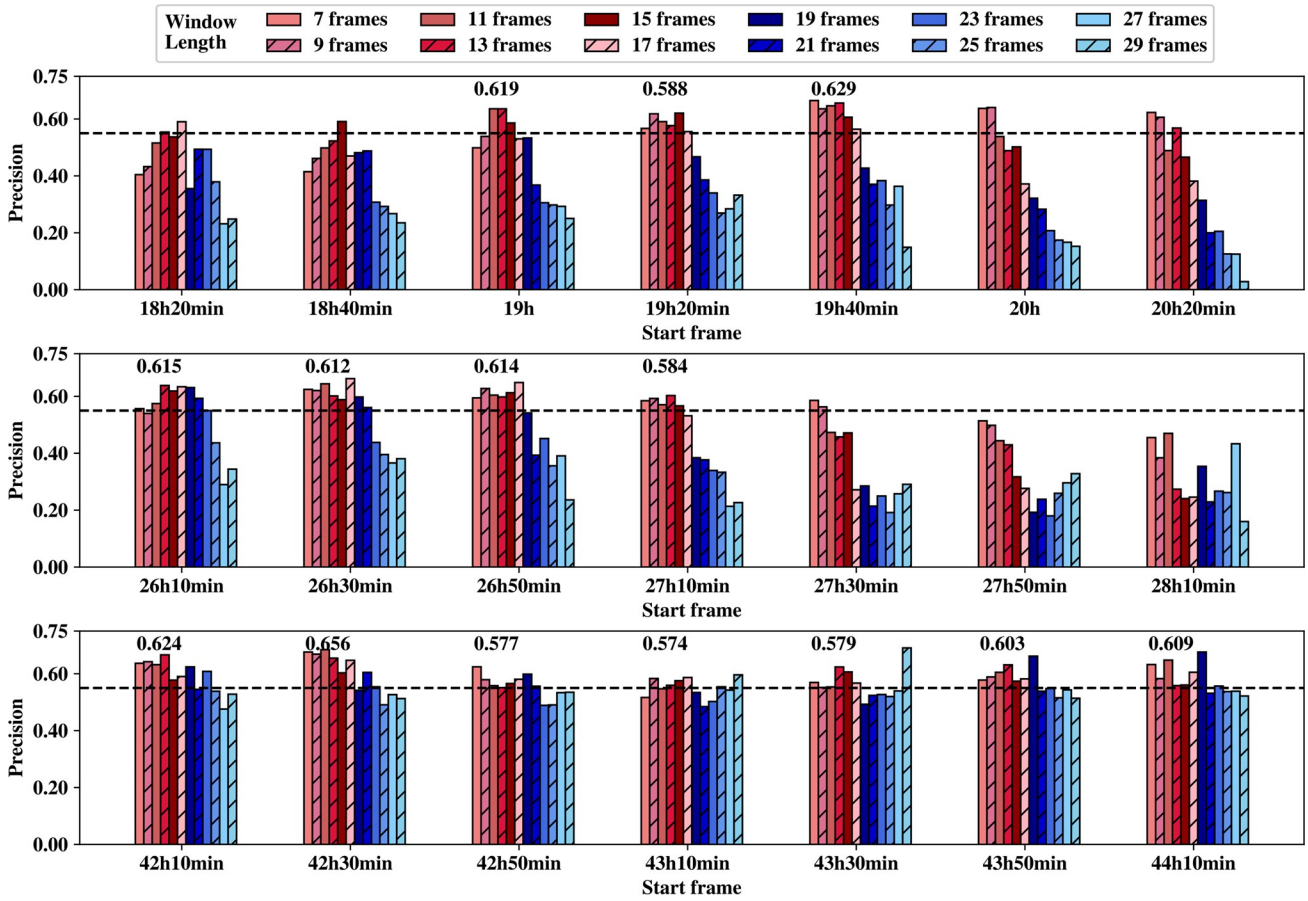

Fig 3. Time window selection. The three subplots represent the precision values for different time windows based on 21 start frames (x axis) and 12 window lengths (7 frames to 29 frames) for phases 1, 2, and 3 (from top to bottom) respectively, and the black bash line in each subplot indicates a precision value of 0.55.

https://doi.org/10.1371/journal.pcbi.1007351.g003

The model performance on these different time windows is shown in Fig 3. In this figure, shorter window lengths are marked in red colors and longer window lengths are marked in blue colors. We observe that precision of longer window lengths is lower than that of shorter window lengths in three phases, and this trend is less pronounced for phase 3. The size of the dataset may be the major reason for this trend. Due to the two rules in dataset generation, the amount of samples satisfying conditions decreases gradually with the increasing window length. For window length of 29 frames, there are just about 38 iPS progenitor cells and 262 normal MEFs in phase 1, about 44 iPS progenitor cells and 283 normal MEFs in phase 2, about 36 iPS progenitor cells and 242 normal MEFs in phase 3. As compared with the window length of 7 frames, there are about 53 iPS progenitor cells and 290 normal MEFs in phase 1, about 55 iPS progenitor cells and 285 normal MEFs in phase 2, about 57 iPS progenitor cells and 300 normal MEFs in phase 3. On the other hand, the number of samples is much less for later start frame than that for previous time since some cells have divided. For instance, there are only about 30 iPS progenitor cells and 200 normal MEFs for the last start frame with length of 29 frames in phase 3.

Selection of best time windows according to maximum precision results in an unstable prediction performance. For instance, precision achieves the maximum value on the time window starting at 43h30min with length of 29 frames while all its adjacent time windows have poor

performance with lower precision. It is unlikely to achieve the same performance on a new dataset of the same time window.

We selected the best start frame for each phase respectively. To exclude the start frame with high prediction precision for only 1 or 2 window lengths, 14 candidates of best start frames were selected when precision was above 0.55 for at least three successive window lengths. For each candidate best start frame, the average precision was calculated over the successive window lengths whose precision was above 0.55 and the average precision values were shown above each candidate best start frame in Fig 3. We only selected one best start frame for each phase according to the average precision values of the candidate best start frames, resulted in 19h40min, 26h10min and 42h30min for phases 1, 2 and 3, respectively.

Secondly, the candidate best window lengths were selected whose precision values were all above 0.55 for 3 best start frames of step 1, resulting in window lengths 11, 13, 15 and 17 frames. For each window length, the precision values, average precision and the corresponding standard deviation of 3 different best start frames were provided in Table A of S1 File. The average precision of 0.640 for window length of 13 frame was the highest while its standard deviation was the smallest (0.01), thus window length of 13 frames was selected as the best window length.

Two-step feature selection

We performed a two-step feature selection method on three phases respectively. Firstly, we generated datasets from best time windows based on the training cell image datasets. The dataset of each phase contained 11 types of morphological and motion features, all of which contained about 50~59 iPS progenitor cells and about 200~295 normal MEFs.

For the first step, an iterative feature removal procedure was performed on the corresponding dataset of each phase to study the importance of each feature type. Average precision was calculated via 5-fold cross-validation over 20 runs on the dataset of each phase, and later set as initial unimportance score. Next, we removed each type of features and calculated the unimportance scores (average precision). Feature with maximum score would be deleted only if this score was greater than the initial unimportance score, which would then be updated as the maximum score. This step was repeated until no score was greater than initial score or no more feature could be selected.

Results from step 1 feature selection are shown in Fig 4. For phase 1 precision is no longer improving after removing ellipsoid-oblate, displacement and volume; for phase 2 precision is no longer improving after removing displacement and volume; for phase 3 precision is no longer improving after removing displacement, ellipsoid-prolate, area and volume. In the end, eight types of features are selected for phase 1, nine types of features are retained for phase 2, and seven types of features are retained for phase 3. Selected features from this step are indicated in Fig 4 by star symbols. The corresponding precision values for best windows with 13 frames before feature selection are 0.624, 0.607, 0.646 for phases 1, 2 and 3, respectively, and after feature selection, these precision values have increased to 0.691, 0.613 and 0.682 respectively.

The removing order of feature type in Fig 4 indicates the importance of each feature type. We observe from Fig 4 that three types of features, nucleus-cytoplasm ratio, sphericity and intensity-StdDev, are important among all three phases. Nucleus-cytoplasm ratio is the top important factor in three phases. Sphericity and intensity-StdDev are among the top 4 common features of three phases. Intensity shows clear different patterns between normal MEFs and progenitor cells. As shown in Fig 5A, the progenitor cells in the blue circles show a uniform intensity distribution between nucleus and cytoplasm, while for normal MEFs in the yellow boxes, the cytoplasm shows weaker intensity as indicated by the blurring edges. Also

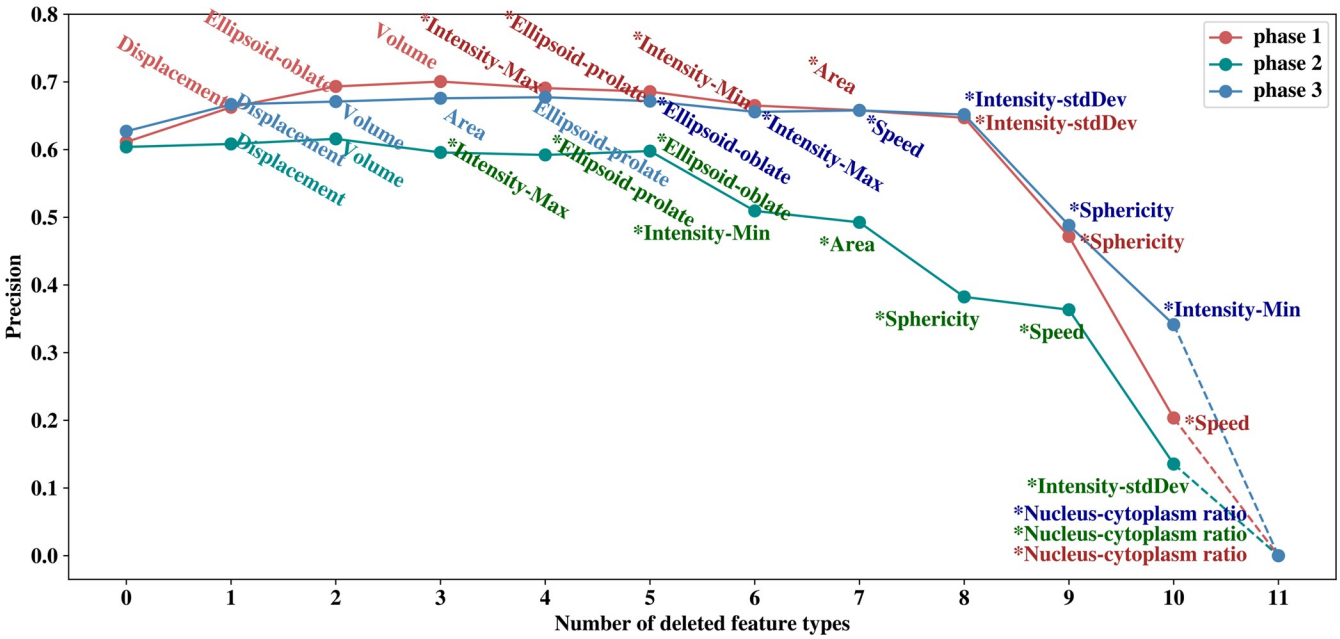

Fig 4. Feature ranking and selection. This figure shows how the precision values change with the deleted feature in a recursive fashion. Least important features are removed earlier.

https://doi.org/10.1371/journal.pcbi.1007351.g004

shown in Fig 5A, the nucleus and cytoplasm of progenitor cells in the blue circles and normal MEFs in the yellow boxes are enlarged and colored by light blue and green respectively. It is clear that nucleus-cytoplasm ratio for progenitor cells are much larger than that of normal MEFs. From Fig 5A, the cell area of progenitor cells is also smaller on average than normal MEFs, indicating the importance of sphericity since area is closely related to sphericity by the equation from Part 1 of the S1 File. The selected features are consistent with the experimental results that iPS progenitor cells exhibit higher nucleus-cytoplasm ratio, smaller total area, and higher proliferation rate than normal MEFs [21].

In order to further study the correlations of different features, as a second step we calculated the Pearson correlation coefficients between the selected features. The results for three phases are shown in Fig 5B. In our model, two feature types are considered strongly correlated if the coefficient is greater than 0.6 and one of them was removed. When two different feature types are strongly correlated with a third feature type, both of them are removed with the purpose of keeping as less number of features as possible. For phase 1, the coefficient between sphericity and area is 0.77 in phase 1, and the coefficient between sphericity and ellipsoid-prolate is 0.66, thus area and ellipsoid-prolate are removed from the list. Similarly, they are removed for phase 2 as well. The strong correlation between sphericity, ellipsoid-prolate and area is caused by the fact that Imaris extracts features from two-dimensional cell images assuming cell thickness as constant. Furthermore, since ellipsoid-oblate is associated with cell thickness, it is removed from the feature list as well for phase 2 and phase 3. Overall, six types of features (Sphericity, I-Min, I-stdDev, I-Max, Ratio, Speed) are selected for all the models.

Cross-validation

With selected features, a grid-search scheme was used for hyperparameter optimization of XGBoost with 5-fold cross-validation, and the datasets were generated based on the training sets for three phases. Three hyperparameters such as learning_rate, n_estimators and gamma

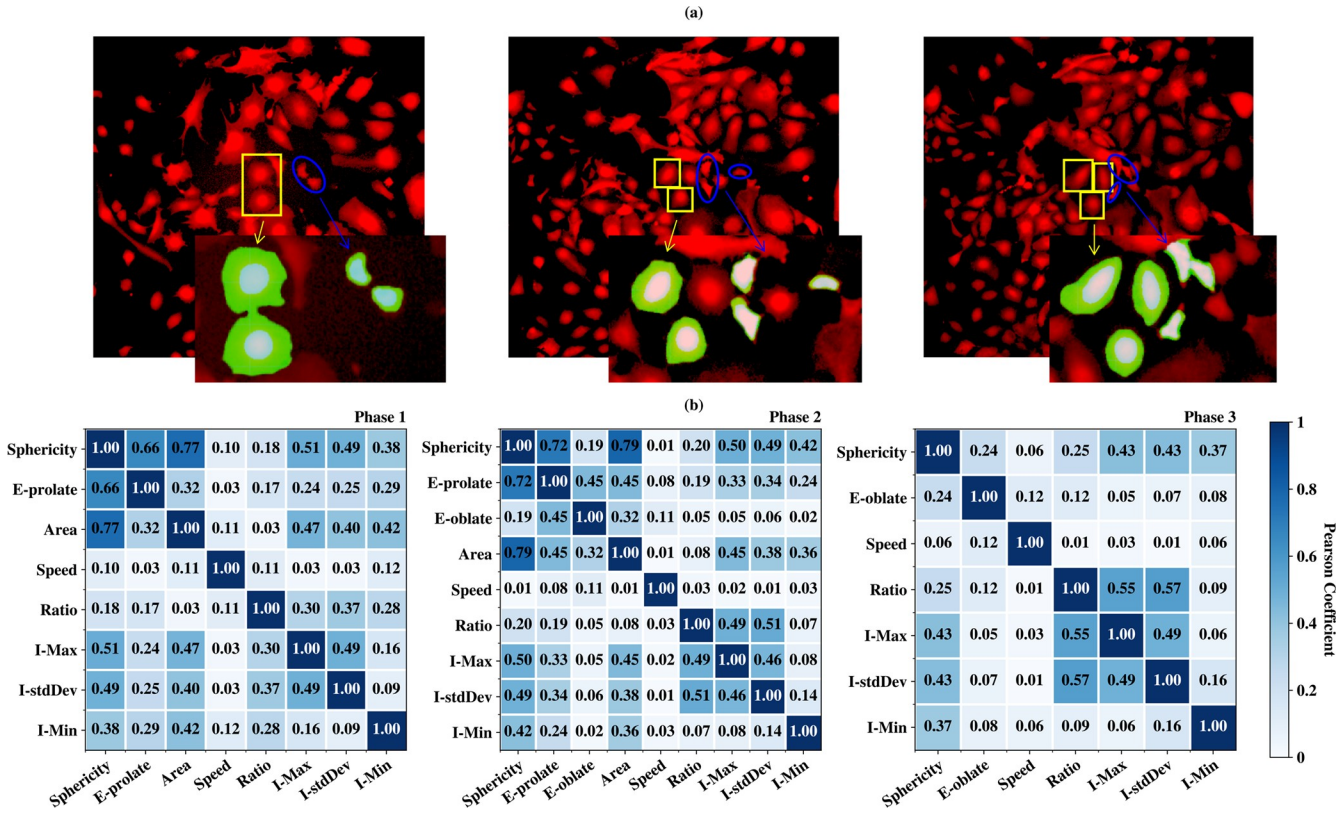

Fig 5. iPS progenitor cells vs. MEFs and feature correlation. (a) shows the examples of iPS progenitor cell images (blue circles) and normal MEFs images (yellow boxes) taken from phase 1, 2 and 3 of field 2 (Left, middle and right). Nucleus and cytoplasm of the enlarged progenitor cells and normal MEFs are colored in light blue and green respectively. (b) shows the Pearson coefficients between remaining types of features in three phases after the first step of feature selection. Note in this figure ellipsoid-prolate is denoted as E-prolate, intensity-StdDev as I-stdDev, intensity-min as I-Min, intensity-max as I-Max, nucleus-cytoplasm volume ratio as Ratio, ellipsoid-oblate as E-oblate.

https://doi.org/10.1371/journal.pcbi.1007351.g005

were set to 0.01, 385 and 0 respectively. We had validated our model with three different experiments as shown in Fig 1.

For cross-validation, datasets were generated from initial whole cell image dataset. Dataset for phase 1 contained about 63 iPS progenitor cells and about 326 normal MEFs. Dataset for phase 2 contained about 82 iPS progenitor cells and about 427 normal MEFs. Dataset for phase 3 contained about 72 iPS progenitor cells and about 359 normal MEFs. For each phase, 5-fold cross validation was performed 10 times on every best time windows with 6 selected feature types, resulting in a total of 117 for window length of 13 frames. Fig 6A shows precision scores for 3 different phases, and all of the precision values are above 0.580. For phase 1, the precision value is highest, 0.732.

Holdout validation

Holdout validation is used to test the model's ability to predict the iPS progenitor cells in the neighborhood of the time window in which the model has been trained. Since in real application, it is difficult to generate the dataset whose images have the exact start time as in the training dataset, holdout-validation is very important for testing the model's generality on the neighborhood time windows. For each phase, the training dataset for window length of 13 frames was generated. In phase 1, the window start frame I was 19h40min as shown in Fig 6D. Models trained on this dataset was then tested on seven test datasets corresponding to start

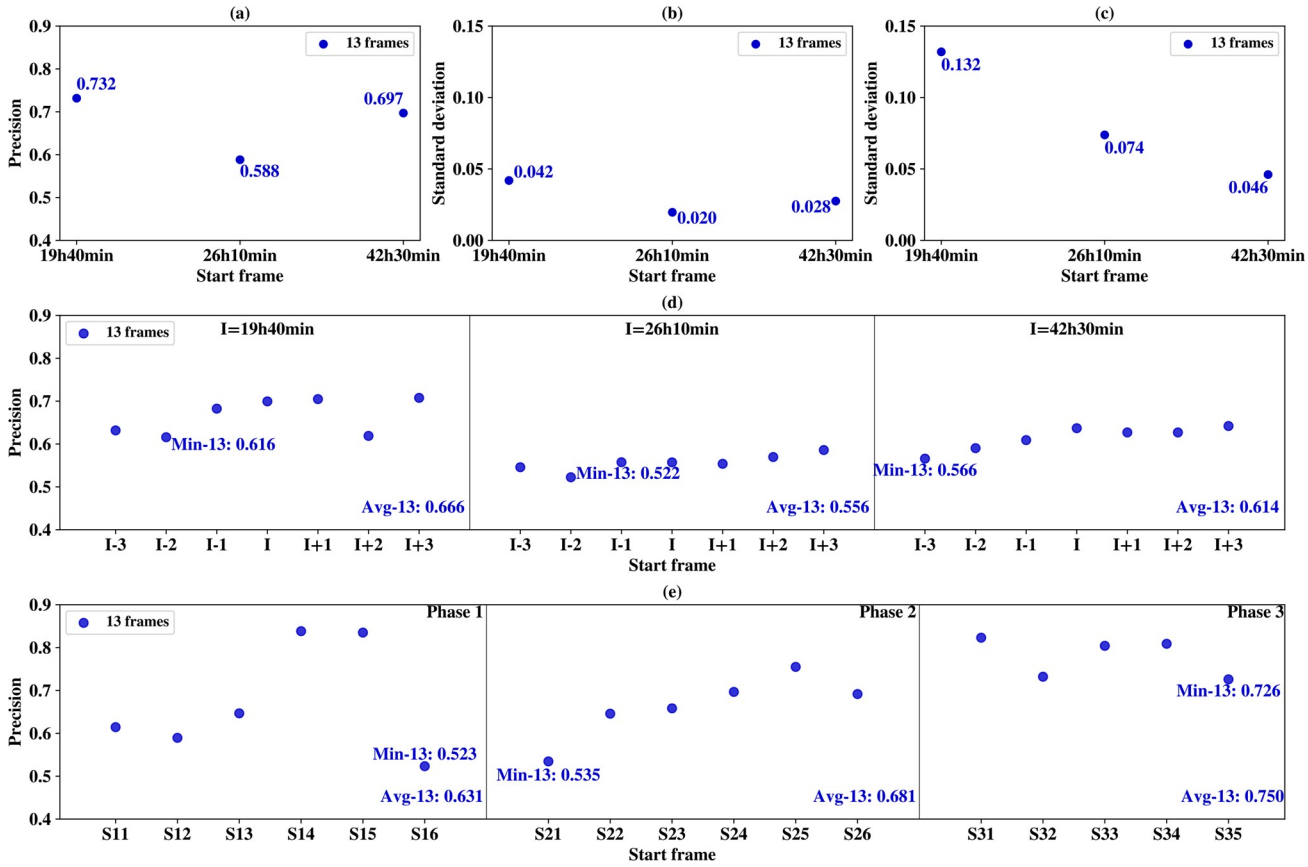

Fig 6. Model validation. In all sub-figures, X axis indicates the start frame of the best time windows and the corresponding window length (13 frames) is indicated in the inlet. (a) 5-fold cross-validation precisions over 10 runs. (b) the standard deviation of the average precision of the neighborhood time windows in Fig 6D. (c) the standard deviation of the average precision of the distant windows in Fig 6E. (d) the average precision of seven neighborhood time windows calculated over 10 holdout validation runs. (e) the average precision over 10 independent tests for six best time windows on their corresponding distant windows.

https://doi.org/10.1371/journal.pcbi.1007351.g006

frames I, I-1, I-2, I-3, I+1, I+2 and I+3, illustrated in Fig 1 and Fig 6D. There was no overlap between the training and testing datasets.

For each time window, average precision value was computed over 10 holdout validation runs, and the results are shown in Fig 6D. The minimum average precision values are 0.616 for window length of 13 frames and start frame I-2 in phase 1, 0.522 for window length of 13 frames and start frame I-2 in phase 2 and 0.566 for window length of 13 frames and start frame I-3 in phase 3. These minimum precisions are all smaller than the corresponding precisions in Fig 6A; what is more, Fig 6D also shows the average precision values for phase 1, 2 and 3 are all smaller than the cross-validation resulted in Fig 6A, indicating the difficulties for predicting in the neighborhood time windows.

For each result of the 3 phases in Fig 6D, the standard deviations of average precision are computed for window length of 13 frames in Fig 6B. The maximum deviation is 0.042 for window length of 13 frames in phase 1 and this indicates the trained models are relatively stable in terms of prediction precision in a wide range of neighborhood windows.

Independent test

Finally, to test the model's ability to predict the iPS progenitor cells on a distant time window without overlapped frames with the training window, we performed an independent test. If

the training cell trajectory is long and contains enough typical iPS progenitor cells, the trained model on one window should be able to identify the motion and morphological patterns of iPS progenitor cells against normal MEFs, regardless of the selected time window.

For phase 1, the model trained on time window 19h40min~21h40min (length of 13 frames) was tested on time windows of phase 2, including time windows starting from 26h20min (S11), 26h40min (S12), 27h (S13), 27h20min (S14), 27h40min (S15), and 28h (S16), shown in the first panel of Fig 6E. Similarly, for phase 2, the model trained on time windows 26h10min~28h10min (length of 13 frames) was tested on six time windows of phase 3 starting from 42h10min (S21), 42h30min (S22), 42h50min (S23), 43h10min (S24), 43h30min (S25), 43h50min (S26), shown in the middle panel of Fig 6E. Lastly, for phase 3, model testing was performed on the distant time windows without overlapped frames from the same phase, shown in the right panel of Fig 6E**.** For time windows 42h30min~44h30min, we selected test time windows starting from 45h10min (S31), 45h30min (S32), 45h50min (S33), 46h10min (S34), 46h30min (S35).

Results of the independent test runs are shown in Fig 6E. The minimum precision is 0.523 for window length of 13 frames for S16 in phase 1. The average precision of phase 1 is lower than those of holdout validation and cross-validation, however, the average precision of phase 2 and 3 are both better than cross-validation and holdout validation. For the prediction of distant time windows, our model could have worse performance than that of neighborhood windows, but our model could also outperform the cross validation and holdout validation (indicated by the standard deviation in Fig 6C). The reason is the independent test datasets for phase 2 and 3 are closely related to the training dataset. The standard deviations of the independent tests are much higher than those of the holdout validation, which could also be seen from the large fluctuations of the precision values in Fig 6E. Nevertheless, the minimum average prediction precision is above 52% among all the experiments, and maximum average precision is about 0.750 for the independent test in phase 3.

Conclusion

In this paper, we proposed a machine learning based model together with time-lapse image analysis to predict/identify iPS progenitor cells during the first 3–5 days after reprogramming initiation. The model generated a variety of morphological and motion features among different time windows, then relied on a two-step feature selection algorithm to select the most important features. The proposed computational approach is very unique from previous experimental techniques which identify the iPS progenitor cells by retrospectively tracking the cell images manually frame by frame from the image frame of GFP expression.

By the experimental study of the enriched iPS progenitor cells in the early stage of reprogramming, the proposed method could provide a new technique or attempt for experimenters to improve the iPS reprogramming efficiency and to study the underlying mechanism of iPS reprogramming. Morphological and motion features, especially sphericity, intensity-StdDev and nucleus-cytoplasm volume ratio, have been found most important for the progenitor cell classification, which is consistent with the experimental observations.

Cross-validation of the proposed method trained and tested on the same time window shows that the prediction precision is above 0.580 for all three phases. Since in real applications, it is very difficult to match imaging timeline precisely between different experiments, holdout validation and an independent test are also performed to test the model's ability to predict iPS progenitor cells in the neighborhood time windows and distant time windows, respectively. The results show our model can predict the iPS progenitor cells with a minimum precision of 52% for neighborhood windows and distant windows, and the maximum average

precision is about 0.750 for the independent test in phase 3. The prediction performance of our model tends to have a larger fluctuation for distant windows than for neighborhood windows, indicated by the larger standard deviation of independent test runs.

For future works, models on different time windows for each phase can be combined to achieve higher prediction accuracy.

Supporting information

S1 File. Supplementary material.
(DOC)

Author Contributions

Conceptualization: Yin Peng, Hongchang Li, Yanjie Wei.

Data curation: Haishan Zhang, Yanning Teng.

Formal analysis: Haishan Zhang.

Funding acquisition: Yanjie Wei.

Investigation: Haishan Zhang, Ximing Shao.

Methodology: Haishan Zhang, Yin Peng.

Project administration: Yanjie Wei.

Resources: Ximing Shao.

Software: Haishan Zhang.

Supervision: Yin Peng, Yanjie Wei.

Validation: Haishan Zhang.

Visualization: Haishan Zhang.

Writing – original draft: Haishan Zhang, Ximing Shao.

Writing – review & editing: Yin Peng, Konda Mani Saravanan, Huiling Zhang, Hongchang Li, Yanjie Wei.

References

1. Takahashi K, Yamanaka S. Induction of pluripotent stem cells from mouse embryonic and adult fibroblast cultures by defined factors. Cell. 2006; 126(4):663–76. https://doi.org/10.1016/j.cell.2006.07.024 PMID: 16904174
2. Yamanaka S. Induced pluripotent stem cells: past, present, and future. Cell Stem Cell. 2012; 10 (6):678–84. https://doi.org/10.1016/j.stem.2012.05.005 PMID: 22704507
3. Takayama N, Nishimura S, Nakamura S, Shimizu T, Ohnishi R, Endo H, et al. Transient activation of c-MYC expression is critical for efficient platelet generation from human induced pluripotent stem cells. J Exp Med. 2010; 207(13):2817–30. https://doi.org/10.1084/jem.20100844 PMID: 21098095
4. Nori S, Okada Y, Yasuda A, Tsuji O, Takahashi Y, Kobayashi Y, et al. Grafted human-induced pluripotent stem-cell-derived neurospheres promote motor functional recovery after spinal cord injury in mice. Proc Natl Acad Sci U S A. 2011; 108(40):16825–30. https://doi.org/10.1073/pnas.1108077108 PMID: 21949375
5. Okamoto S, Takahashi M. Induction of retinal pigment epithelial cells from monkey iPS cells. Invest Ophthalmol Vis Sci. 2011; 52(12):8785–90. https://doi.org/10.1167/iovs.11-8129 PMID: 21896853
6. Kriks S, Shim JW, Piao J, Ganat YM, Wakeman DR, Xie Z, et al. Dopamine neurons derived from human ES cells efficiently engraft in animal models of Parkinson's disease. Nature. 2011; 480 (7378):547–51. https://doi.org/10.1038/nature10648 PMID: 22056989

7. Israel MA, Yuan SH, Bardy C, Reyna SM, Mu Y, Herrera C, et al. Probing sporadic and familial Alzheimer's disease using induced pluripotent stem cells. Nature. 2012; 482(7384):216–20. https://doi.org/10.1038/nature10821 PMID: 22278060
8. Ben-David U, Benvenisty N. The tumorigenicity of human embryonic and induced pluripotent stem cells. Nat Rev Cancer. 2011; 11(4):268–77. https://doi.org/10.1038/nrc3034 PMID: 21390058
9. Kanemura H, Go MJ, Shikamura M, Nishishita N, Sakai N, Kamao H, et al. Tumorigenicity studies of induced pluripotent stem cell (iPSC)-derived retinal pigment epithelium (RPE) for the treatment of age-related macular degeneration. PLoS One. 2014; 9(1):e85336. https://doi.org/10.1371/journal.pone.0085336 PMID: 24454843
10. Okita K, Ichisaka T, Yamanaka S. Generation of germline-competent induced pluripotent stem cells. Nature. 2007; 448(7151):313–7. https://doi.org/10.1038/nature05934 PMID: 17554338
11. Sridharan R, Tchieu J, Mason MJ, Yachechko R, Kuoy E, Horvath S, et al. Role of the murine reprogramming factors in the induction of pluripotency. Cell. 2009; 136(2):364–77. https://doi.org/10.1016/j.cell.2009.01.001 PMID: 19167336
12. Shu J, Wu C, Wu Y, Li Z, Shao S, Zhao W, et al. Induction of pluripotency in mouse somatic cells with lineage specifiers. Cell. 2013; 153(5):963–75. https://doi.org/10.1016/j.cell.2013.05.001 PMID: 23706735
13. Cacchiarelli D, Trapnell C, Ziller MJ, Soumillon M, Cesana M, Karnik R, et al. Integrative Analyses of Human Reprogramming Reveal Dynamic Nature of Induced Pluripotency. Cell. 2015; 162(2):412–24. https://doi.org/10.1016/j.cell.2015.06.016 PMID: 26186193
14. He X, Cao Y, Wang L, Han Y, Zhong X, Zhou G, et al. Human fibroblast reprogramming to pluripotent stem cells regulated by the miR19a/b-PTEN axis. PLoS One. 2014; 9(4):e95213. https://doi.org/10.1371/journal.pone.0095213 PMID: 24740298
15. Huh S, Song HR, Jeong GR, Jang H, Seo NH, Lee JH, et al. Suppression of the ERK-SRF axis facilitates somatic cell reprogramming. Exp Mol Med. 2018; 50(2):e448. https://doi.org/10.1038/emm.2017.279 PMID: 29472703
16. Miles DC, de Vries NA, Gisler S, Lieftink C, Akhtar W, Gogola E, et al. TRIM28 is an Epigenetic Barrier to Induced Pluripotent Stem Cell Reprogramming. Stem Cells. 2017; 35(1):147–57. https://doi.org/10.1002/stem.2453 PMID: 27350605
17. Polo JM, Anderssen E, Walsh RM, Schwarz BA, Nefzger CM, Lim SM, et al. A molecular roadmap of reprogramming somatic cells into iPS cells. Cell. 2012; 151(7):1617–32. https://doi.org/10.1016/j.cell.2012.11.039 PMID: 23260147
18. Dabiri Y, Gama-Brambila RA, Taskova K, Herold K, Reuter S, Adjaye J, et al. Imidazopyridines as Potent KDM5 Demethylase Inhibitors Promoting Reprogramming Efficiency of Human iPSCs. iScience. 2019; 12:168–81. https://doi.org/10.1016/j.isci.2019.01.012 PMID: 30685712
19. Hong H, Takahashi K, Ichisaka T, Aoi T, Kanagawa O, Nakagawa M, et al. Suppression of induced pluripotent stem cell generation by the p53-p21 pathway. Nature. 2009; 460(7259):1132–5. https://doi.org/10.1038/nature08235 PMID: 19668191
20. Robertson A, Mohamed TM, El Maadawi Z, Stafford N, Bui T, Lim DS, et al. Genetic ablation of the mammalian sterile-20 like kinase 1 (Mst1) improves cell reprogramming efficiency and increases induced pluripotent stem cell proliferation and survival. Stem Cell Res. 2017; 20:42–9. https://doi.org/10.1016/j.scr.2017.02.011 PMID: 28257933
21. Smith ZD, Nachman I, Regev A, Meissner A. Dynamic single-cell imaging of direct reprogramming reveals an early specifying event. Nat Biotechnol. 2010; 28(5):521–6. https://doi.org/10.1038/nbt.1632 PMID: 20436460
22. Zhang J, Nuebel E, Daley GQ, Koehler CM, Teitell MA. Metabolic regulation in pluripotent stem cells during reprogramming and self-renewal. Cell Stem Cell. 2012; 11(5):589–95. https://doi.org/10.1016/j.stem.2012.10.005 PMID: 23122286
23. Li R, Liang J, Ni S, Zhou T, Qing X, Li H, et al. A mesenchymal-to-epithelial transition initiates and is required for the nuclear reprogramming of mouse fibroblasts. Cell Stem Cell. 2010; 7(1):51–63. https://doi.org/10.1016/j.stem.2010.04.014 PMID: 20621050
24. Megyola CM, Gao Y, Teixeira AM, Cheng J, Heydari K, Cheng EC, et al. Dynamic migration and cell-cell interactions of early reprogramming revealed by high-resolution time-lapse imaging. Stem Cells. 2013; 31(5):895–905. https://doi.org/10.1002/stem.1323 PMID: 23335078
25. Dufour A, Thibeaux R, Labruyere E, Guillen N, Olivo-Marin JC. 3-D active meshes: fast discrete deformable models for cell tracking in 3-D time-lapse microscopy. IEEE Trans Image Process. 2011; 20(7):1925–37. https://doi.org/10.1109/TIP.2010.2099125 PMID: 21193379
26. Dzyubachyk O, van Cappellen WA, Essers J, Niessen WJ, Meijering E. Advanced level-set-based cell tracking in time-lapse fluorescence microscopy. IEEE Trans Med Imaging. 2010; 29(3):852–67. https://doi.org/10.1109/TMI.2009.2038693 PMID: 20199920

27. Maska M, Danek O, Garasa S, Rouzaut A, Munoz-Barrutia A, Ortiz-de-Solorzano C. Segmentation and shape tracking of whole fluorescent cells based on the Chan-Vese model. IEEE Trans Med Imaging. 2013; 32(6):995–1006. https://doi.org/10.1109/TMI.2013.2243463 PMID: 23372077

28. Türetken E, Wang X, Becker CJ, Haubold C, Fua P. Network Flow Integer Programming to Track Elliptical Cells in Time-Lapse Sequences. IEEE Transactions on Medical Imaging. 2017; 36(4):942–51. https://doi.org/10.1109/TMI.2016.2640859 PMID: 28029619

29. Payer C, Štern D, Neff T, Bischof H, Urschler M, editors. Instance Segmentation and Tracking with Cosine Embeddings and Recurrent Hourglass Networks. Medical Image Computing and Computer Assisted Intervention–MICCAI 2018; 2018 2018//; Cham: Springer International Publishing.

30. Erdmann G, Volz C, Boutros M. Systematic approaches to dissect biological processes in stem cells by image-based screening. Biotechnol J. 2012; 7(6):768–78. https://doi.org/10.1002/biot.201200117 PMID: 22653826

31. Van Valen DA, Kudo T, Lane KM, Macklin DN, Quach NT, DeFelice MM, et al. Deep Learning Automates the Quantitative Analysis of Individual Cells in Live-Cell Imaging Experiments. PLoS Comput Biol. 2016; 12(11):e1005177. https://doi.org/10.1371/journal.pcbi.1005177 PMID: 27814364

32. Chen CL, Mahjoubfar A, Tai LC, Blaby IK, Huang A, Niazi KR, et al. Deep Learning in Label-free Cell Classification. Sci Rep. 2016; 6:21471. https://doi.org/10.1038/srep21471 PMID: 26975219

33. Kraus OZ, Grys BT, Ba J, Chong Y, Frey BJ, Boone C, et al. Automated analysis of high-content microscopy data with deep learning. Mol Syst Biol. 2017; 13(4):924. https://doi.org/10.15252/msb.20177551 PMID: 28420678

34. Gao Z, Wang L, Zhou L, Zhang J. HEp-2 Cell Image Classification With Deep Convolutional Neural Networks. IEEE J Biomed Health Inform. 2017; 21(2):416–28. https://doi.org/10.1109/JBHI.2016.2526603 PMID: 26887016

35. Stumpf PS, MacArthur BD. Machine Learning of Stem Cell Identities From Single-Cell Expression Data via Regulatory Network Archetypes. Front Genet. 2019; 10:2. https://doi.org/10.3389/fgene.2019.00002 PMID: 30723489

36. Chen T, Guestrin C. XGBoost: A Scalable Tree Boosting System. Proceedings of the 22nd ACM SIGKDD International Conference on Knowledge Discovery and Data Mining—KDD '162016. p. 785–94.

37. Chen J, Liu J, Chen Y, Yang J, Chen J, Liu H, et al. Rational optimization of reprogramming culture conditions for the generation of induced pluripotent stem cells with ultra-high efficiency and fast kinetics. Cell Res. 2011; 21(6):884–94. https://doi.org/10.1038/cr.2011.51 PMID: 21445094

38. Esteban MA, Wang T, Qin B, Yang J, Qin D, Cai J, et al. Vitamin C enhances the generation of mouse and human induced pluripotent stem cells. Cell Stem Cell. 2010; 6(1):71–9. https://doi.org/10.1016/j.stem.2009.12.001 PMID: 20036631

39. Aibar S, González-Blas CB, Moerman T, Huynh-Thu VA, Imrichova H, Hulselmans G, et al. SCENIC: single-cell regulatory network inference and clustering. Nature Methods. 2017; 14:1083. https://doi.org/10.1038/nmeth.4463 PMID: 28991892

40. Li H, Pang F, Shi Y, Liu Z. Cell dynamic morphology classification using deep convolutional neural networks. Cytometry A. 2018; 93(6):628–38. https://doi.org/10.1002/cyto.a.23490 PMID: 29762901

41. Zhong J, Sun Y, Peng W, Xie M, Yang J, Tang X. XGBFEMF: An XGBoost-Based Framework for Essential Protein Prediction. IEEE Trans Nanobioscience. 2018; 17(3):243–50. https://doi.org/10.1109/TNB.2018.2842219 PMID: 29993553

42. Chen CLP, Zhang T, Chen L, Tam SC. I-Ching Divination Evolutionary Algorithm and its Convergence Analysis. IEEE Transactions on Cybernetics. 2017; 47(1):2–13. https://doi.org/10.1109/TCYB.2015.2512286 PMID: 26800558

43. Zhang T, Chen CLP, Chen L, Xu X, Hu B. Design of Highly Nonlinear Substitution Boxes Based on I-Ching Operators. IEEE Transactions on Cybernetics. 2018; 48(12):3349–58. https://doi.org/10.1109/TCYB.2018.2846186 PMID: 30040668